

Variable structure in the PDS 70 disc and uncertainties in radio-interferometric image restoration

Simon Casassus,^{1,2,3*} Miguel Cárcamo,^{4,5,6}

¹ *Departamento de Astronomía, Universidad de Chile, Casilla 36-D, Santiago, Chile*

² *Facultad de Ingeniería y Ciencias, Universidad Adolfo Ibáñez, Av. Diagonal las Torres 2640, Peñalolén, Santiago, Chile*

³ *Data Observatory Foundation, Chile*

⁴ *Jodrell Bank Centre for Astrophysics, Department of Physics and Astronomy, University of Manchester, Alan Turing Building, Oxford Road, Manchester, M13 9PL, UK*

⁵ *University of Santiago of Chile (USACH), Faculty of Engineering, Computer Engineering Department, Chile*

⁶ *Center for Interdisciplinary Research in Astrophysics and Space Exploration (CIRAS), Universidad de Santiago de Chile*

Accepted XXX. Received YYY; in original form ZZZ

ABSTRACT

The compact mm-wavelength signal in the central cavity of the PDS 70 disc, revealed by deep ALMA observations, is aligned with unresolved H α emission, and is thought to stem from a circum-planetary disc (CPD) around PDS 70c. We revisit the available ALMA data on PDS 70c with alternative imaging strategies, and with special attention to uncertainties and to the impact of the so-called “JvM correction”, which is thought to improve the dynamic range of restored images. We also propose a procedure for the alignment and joint imaging of multi-epoch visibility data. We find that the JvM correction exaggerates the peak signal-to-noise of the data, by up to a factor of 10. In the case of PDS 70, we recover the detection of PDS 70c from the July 2019 data, but only at 8σ . However, its non-detection in Dec. 2017 suggests that PDS 70c is variable by at least $42\% \pm 13\%$ over a 1.75 yr time-span, so similar to models of the H α variability. We also pick up fine structure in the inner disc, such that its peak is offset by $\sim 0''.04$ from the disc centre. The inner disc is variable too, which we tentatively ascribe to Keplerian rotation as well as intrinsic morphological changes.

Key words: techniques: interferometric – protoplanetary discs – planets and satellites: formation – stars: individual: PDS 70

1 INTRODUCTION

The accretion of giant planets in circum-stellar discs is thought to be regulated by a circum-planetary disc (CPD), which is fed by intricate flows inside planetary wakes (e.g. Szulágyi & Ercolano 2020). However, CPD detections have been remarkably elusive, except for the compact vibrational CO signal detected in the central cavity of HD 100546 by (Brittain et al. 2019), or the near-IR black-body component required to account for the spectral energy distribution of PDS 70b (Christiaens et al. 2019). In general such CPDs are expected to be faint compact sources, up to one Hill radius wide and surrounded by complex structures in the parent disc (e.g. Szulágyi et al. 2018). The search for CPDs with ALMA thus requires bringing the instruments to its limits, and a very good knowledge of the uncertainties in the resulting images so as to pick-up genuine signal.

Long-baseline ALMA observations of the PDS 70 disc revealed the detection of a compact source inside the cen-

tral cavity (Benisty et al. 2021), closely aligned with unresolved H α signal probably associated to an accreting protoplanet (i.e. PDS 70c, Haffert et al. 2019). The compact mm-wavelength signal may thus stem from a CPD around PDS 70c (Benisty et al. 2021). However, the data analysis rests on the “JvM correction” (Jorsater & van Moorsel 1995; Czekala et al. 2021), an image restoration procedure that is thought to improve dynamic range. Image restoration, applicable to all synthesis imaging techniques, allows to convey uncertainties, and to recover faint signal that may have been missed by model images.

The direct detection of a CPD, thanks to deep ALMA observations, is a momentous achievement in planetary sciences, whose relevance motivates us to revisit these data with alternative synthesis imaging tools. Here we perform non-parametric image synthesis using the UVMEM package (Casassus et al. 2006; Cárcamo et al. 2018) as an alternative to the more commonly used CLEAN algorithm (Högbom 1974; Rau & Cornwell 2011). We give special attention to the alignment of multi-epoch visibility data, and to the impact of the JvM correction.

* E-mail: simon@das.uchile.cl

Our approach to the alignment of the multi-epoch visibility data is described in Sec. 2, and is applied to UVMEM imaging of PDS 70 in Sec. 3. Sec. 4 summarizes our results. Appendix A describes the standard techniques of image restoration and visibility gridding, before showing that the JvM correction exaggerates the sensitivity of restored images.

2 ALIGNMENT OF VISIBILITY DATA

Datasets obtained with different source acquisitions, i.e. multi-epoch observations, may have different absolute flux scales or be affected by different pointing errors. For instance, the flux calibration accuracy for ALMA is thought to be around $\sim 10\%$, and the phase center accuracy (absolute positional accuracy) is, very approximately, about $1/10$ the size of the clean beam major axis (see for instance Remijan et al. 2019). In order to restore images using concatenated datasets, it is necessary to align them. It is also necessary to scale them in flux, as otherwise different flux calibrations will lead to stronger residuals.

Here we propose to align such datasets in the uv -plane, assuming that the source is not variable in time. The result of our procedure is similar to that of joint self-calibration (described in Sec. 3.1), but it restricts the number of unknowns to only a single position shift and a flux scale factor, while self-calibration adjusts time-series for the antenna gains. Another difference is that self-calibration requires a bright source to define an adequate self-calibration model. We describe our procedure for two datasets, labeled S and L anticipating the application to PDS 70, where the datasets correspond to different array configurations, with shorter and longer baselines¹. We extract subsets of each dataset with exactly the same spectral domains in LSRK. We then gridd each dataset to a common uv -grid, in natural weights, so according to Eqs. A3 and A5 (which are implemented in the PYRALYSIS² software package). This results in visibilities $\{\tilde{V}_k^S\}_{k=1}^N$ and $\{\tilde{V}_k^L\}_{k=1}^N$, for the short and long baseline datasets, respectively. The common uv -grid is set by the shortest and longest baselines. We then aligned each pair by shifting \tilde{V}^S , i.e. by minimising

$$\chi_{\text{align}}^2(\alpha_R, \delta\vec{x}) = \sum_{k=1}^N W_k^{\text{align}} \|\tilde{V}_k^L - \tilde{V}_k^{Lm}\|^2, \quad (1)$$

where

$$\tilde{V}_k^{Lm} = \alpha_R e^{i2\pi \delta\vec{x} \cdot \vec{u}_k} \tilde{V}_k^S, \quad (2)$$

corresponds to a spatial shift in origin by $\delta\vec{x}$ and to a scaling of the absolute fluxes for \tilde{V}^S by $\alpha_R \in \mathbb{R}$. The weights are

$$W_k^{\text{align}} = \frac{W_k^S W_k^L}{W_k^S + W_k^L}, \quad (3)$$

where W_k^S and W_k^L are each given by Eq. A4, for both datasets. The overlap in uv -radii, over which the optimisation was carried out, was determined by taking azimuthal averages in the gridded weights W^S and W^L , and selecting

the range where the radial profiles are both above $1/10$ their peak. See Sec. 3.1 below for an example application and for independent checks on the alignment procedure. This visibility alignment procedure is implemented in the package VISALIGN³.

3 APPLICATION TO PDS 70

3.1 Imaging

We refer to Long et al. (2018), Keppler et al. (2019), Isella et al. (2019) and Benisty et al. (2021) for a description of the observations. We followed the same procedures for the extraction of the continuum visibility data, and adopt the same nomenclature as in Benisty et al. (2021) to refer to the various datasets. In summary, we used the datasets corresponding to the following ALMA programmes: 2015.1.00888.S, from August 2016, with short baselines (15 m to 1.5 km) and referred to as SB16; 2017.A.00006.S, from Dec. 2017, with intermediate baselines (15 m and 6.9 km) and referred to as IB17; and 2018.A.00030.S, from July 2019, with long baselines (92 m to 8.5 km) and referred to as LB19.

Provided with the continuum visibility data, we proceeded to self-calibrate (e.g. Cornwell & Fomalont 1999) each dataset independently. For bright sources this procedure improves calibration and may allow reaching thermal noise in the restored image. Given that Benisty et al. (2021) used the JvM correction, in order to set a comparison point before investigating alternative imaging strategies, we first applied the standard self-calibration procedure, as implemented in CASA, and composed of successive iterations of the tasks `tclean`, `gaincal` and `applycal`. We combined all spectral windows (spws), proceeding as in Benisty et al. (2021), and reached a peak signal to noise ratio (PSNR) in the final restored images of 36.3 using Briggs weighting with $r = 2$.

As an alternative imaging strategy, we used the UVMEM package to replace the `tclean` model in the CASA selfcal loop (see Casassus et al. 2018, 2019a, 2021b, for more details on UVMEM and recent applications to ALMA data of protoplanetary discs). We used an elliptical mask enclosing the source that restricts the number of free parameters (as in Casassus et al. 2021b, who used Keplerian masks for line data). For very bright and compact sources, as in SB16 or IB17, this mask is redundant in terms of the final PSNR, but it helps in case of lower dynamic range, as for LB19. For all datasets, we used a pure least-squared (χ^2) optimization, regularized only by the requirement of image positivity (i.e. no entropy term was applied). We then proceeded to self-calibrate the data using a special purpose programming framework, OOSELF-CAL⁴, which is essentially a wrapper for CASA tasks `gaincal` and `applycal` and any choice of imager (in this case UVMEM). OOSELF-CAL allows execution with as little user interaction as possible. This framework starts with phase-calibration only, in selfcal iterations that progressively lower the solution interval by half, starting from the scan length (about 50s). These iterations are interrupted when the PSNR⁵ decreases, and the self-calibrated visibility dataset is reverted to the calibration

¹ this alignment procedure can of course be applied to datasets acquired with the same configuration

² see Data Availability

³ see Data Availability

⁴ see Data Availability

⁵ In our framework this PSNR is calculated as the ratio of peak

tables that yielded the highest PSNR. The phase-calibration stage is then followed by a single loop of amplitude and phase self-calibration, also tested for improvement using the PSNR. For LB19 the phase-calibration progressed until the first iteration, which was enough to reach a PSNR of 56 with $r = 2$. For SB16, a PSNR of 266 ($r = 2$) was reached after two phase calibration loops. For IB17, a single iteration in phase yielded a PSNR of 75 ($r = 2$).

Having self-calibrated each dataset independently, they were concatenated for joint imaging. This required alignment to a common reference dataset, for which we chose LB19, both for position and absolute flux calibration. The alignment was achieved in the uv -plane, using VISALIGN (as described in Sec. 2). We therefore assume that the bulk of PDS 70 is not variable between the two epochs⁶. We extracted a frequency domain common to all 3 datasets, in LSRK, and then aligned each pair SB16/LB19 and IB17/LB19. The common uv -grids correspond to 2048×2048 images with pixel sizes of 3 mas and 4 mas, respectively. Fig. 1 shows the visibility amplitudes for the grid corresponding to the IB17/LB19 alignment. For the SB16 and LB19 alignment, the common range in uv -radii extended from $0.17 M\lambda$ to $0.47 M\lambda$. The fit yielded $\delta\vec{x} = (-0''.012 \pm 0''.001, -0''.019 \pm 0''.001)$. The flux scale factor was $\alpha_R = 0.788 \pm 0.004$, which is somewhat smaller than the ratio of flux densities extracted within the mask, of 0.861 ± 0.004 . The LB19 flux density is biased upwards in our pure χ^2 reconstructions, because of the positive-definite noise in the model images. Using entropy regularization resulted in a lower flux density ratio of 0.77 ± 0.004 (but with stronger synthesis imaging artifacts, which is why we use the pure χ^2 versions). For the IB17 and LB19 alignment, uv -range extended from $0.17 M\lambda$ to $0.71 M\lambda$, $\alpha_R = 1.001 \pm 0.002$ and $\delta\vec{x} = (-0''.01401 \pm 0''.0003, -0''.0203 \pm 0''.0004)$. An absolute flux scale difference of $\sim 20\%$ between SB16 and IB17 or LB19 is not surprising for ALMA Band 7 (Francis et al. 2020). The alternative, that the flux of the disc itself is time-variable, is unlikely since the flux scales between IB17 and LB19 are consistent, while the time separations between IB17 and SB16, and between LB19 and IB17, are similar.

The impact of the alignment is summarised in Figs. 2 and 3. Since the source is a fairly axially symmetric disc, albeit projected on the sky, we rotated and compressed the uv -plane to compensate for the disc orientation, with an inclination $i = 130$ deg and PA = 160.4 deg (see below).

As the disc of PDS 70 is essentially a ring, we can use the center of the ring to test the accuracy of our alignment procedure. The MPOLARMAPS package (Casassus et al. 2021b) estimates the disc orientation, under the assumption of axial symmetry, by minimizing the azimuthal dispersion of radial intensity profiles. We compare the LB19 image, in its restored version (see below), with the IB17 model image (see below). For LB19, the best fit orientation corresponds to PA = 160.4 ± 0.08 deg, $i = 130.0 \pm 0.06$ deg, and a ring center

signal in the restored images to the noise in the whole residual image, with a field of view of 4 arcsec in the case of PDS 70

⁶ Since the bulk of the flux density, by far, is dominated by the outer ring, Keplerian rotation could trace an arc of ~ 10 mas in length, subtending an angle of ~ 0.7 deg in azimuth relative to the star. This is a small angular rotation, that probably does not bias the alignment procedure, which fits for a scaling factor and a positional translation

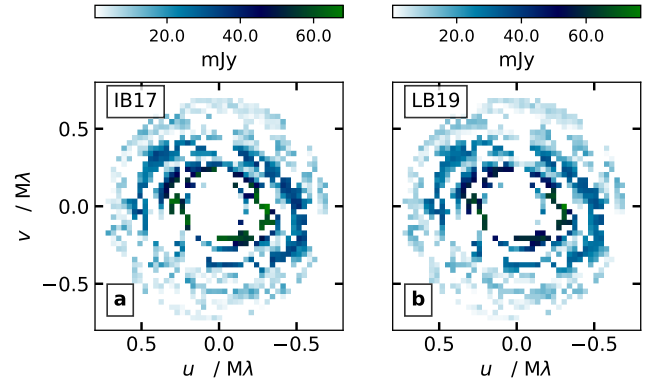


Figure 1. Gridded visibility amplitudes for datasets IB17 (a) and LB19 (b). The data have been filtered for the common uv -domain, according to Eq. 3.

offset by $\vec{\Delta}_{LB19} = (-0''.0018 \pm 0''.0003, -0''.0036 \pm 0''.0003)$ relative to the phase center. For IB17, we obtained PA = 160.5 ± 0.18 deg, $i = 129.9^{+0.16}_{-0.14}$ deg, and a ring center at $\vec{\Delta}_{IB17} = (-0''.0032^{+0''.0006}_{-0''.0009}, -0''.0025 \pm 0''.0008)$ relative to the phase center. The ring centers $\vec{\Delta}_{LB19}$ and $\vec{\Delta}_{IB17}$ coincide within ~ 1 mas, or 1.5σ , in support of the accuracy of the uv -plane alignment with VISALIGN.

Having aligned all 3 datasets, we proceeded with joint imaging. We concatenated the visibility data directly, i.e. with the application of the `statwt` task in CASA to replace the visibility weights by those corresponding to the dispersion of each datum, but without additional modification. We applied the OOSELFICAL framework, which yielded improvements for SB16+IB17+LB19 (PSNR=95) and also for SB16+IB17 (PSNR=94), both after a single round of phase calibration. The amplitude and phase self-calibration resulted in an improvement only for SB16+LB19 (PSNR=84). A selection of images resulting from the present imaging procedure is given in Fig. 4.

3.2 Results and discussion

3.2.1 Noise level in the LB19 image

The noise level reported in Fig. 4a, of $16.4 \mu\text{Jy beam}^{-1}$, appears to match the expected instrumental sensitivity. The ALMA Observing Tool (OT, provided by the Joint ALMA Observatory to prepare ALMA proposals) predicts about 6 h total execution time to reach a noise level of $17 \mu\text{Jy beam}^{-1}$, under default weather conditions. This seems fairly consistent with the actual total execution time for the LB19 dataset, of 3.7h, considering that it was carried out under very good weather conditions (with precipitable water vapour columns ranging from 0.6 to 0.7 mm). However, the noise level quoted by Benisty et al. (2021) for the LB19 dataset using Briggs robustness parameter of 2.0 is only $6.2 \mu\text{Jy beam}^{-1}$, which according to the OT would require 2 d. We suggest that this very low noise level is due to the application of the JvM correction (see Sec. A5).

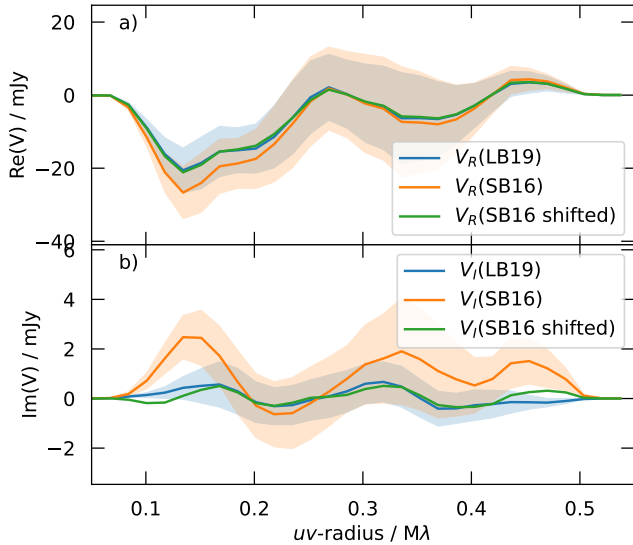


Figure 2. Visibility uv -spectra for SB16 and LB19, and uv -plane alignment. We plot the deprojected and azimuthally-averaged visibilities of PDS 70, over a common range in uv -radii (see text), with real parts in **a**) and imaginary parts in **b**). The total heights of the shaded regions correspond to the standard deviation of azimuthal scatter. We do not plot this scatter for the shifted visibilities to avoid crowding.

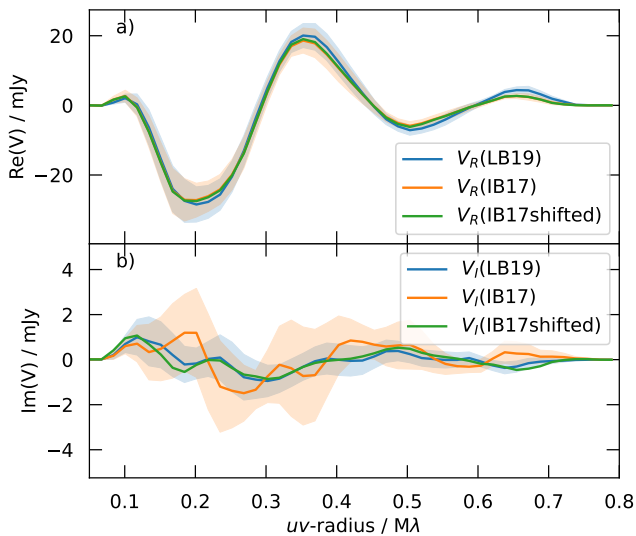


Figure 3. Visibility uv -spectra for IB17 and LB19, and uv -plane alignment. Annotations follow from Fig. 2.

3.2.2 PDS 70c

As summarised in Fig. 4, we confirm the detection of signal coincident with PDS 70c. This is best seen in Fig. 4a, with point-like signal reaching $126 \mu\text{Jy beam}^{-1}$, or 8σ . We note that this point source is surrounded by extended emission, in the form of a filament or spur, that connects with the cavity wall. This spur is best seen in Fig. 4b, where it is detected at 3σ . The color map in Fig. 4 is chosen to highlight the faint fea-

tures and the noise, while also tracing the brighter features. A more standard color map is used in Fig. 5 (the latter version is easier to compare with the color coding used by Benisty et al. 2021, and also with ESO press release eso2111b).

Intriguingly, the point source PDS 70c is missing in LB19+IB17+SB16. In order to test whether this is an effect of averaging different Keplerian rotation phases, we have de-projected the LB19+SB16 data, transformed the map by Keplerian rotation over a period of 1.75 yr around a $0.9 M_{\odot}$ star, re-projected onto the sky plane and averaged the result with the initial image. Fig. 5 shows that, while PDS 70c is somewhat fainter in the average than in the initial image, it is still quite conspicuous.

The absence of PDS 70c in LB19+IB17+SB16 may perhaps reflect that the signal detected in LB19 has been averaged with its absence in IB17. To test this hypothesis we also imaged SB16+IB17, as shown in Fig. 4d, e and f. The noise level in Fig. 4e being $31.9 \mu\text{Jy beam}^{-1}$, and since the data are aligned in position and flux, a $126 \mu\text{Jy}$ point source should have been picked up at 4σ . Instead, the intensity at the location of PDS 70c is $-51 \mu\text{Jy beam}^{-1}$. In order to test for synthesis imaging limitations due to the vicinity of the strong and extended emission from the cavity wall, we injected 4 point sources in the residual visibility data, at the expected location of PDS 70c, and at symmetrical positions relative to the disc axes. As summarised in Fig. 6, the corresponding restored image is consistent a $126 \mu\text{Jy}$ point source at all 4 locations within 2σ .

The absence of PDS 70c in IB17 suggests that it is a variable source. Isella et al. (2019) reported the detection of sub-mm continuum associated to PDS 70c, using the same dataset, but from their Fig. 8 it seems to be offset northwards of the $\text{H}\alpha$ peak. Also, their astrometry is tied to the central continuum peak, which may be offset from the star (see below). In the insets of Figs. 4d and e there are indeed filaments, or spurs, protruding away from the cavity edge more or less at the position of the clump reported by Isella et al. (2019), but they do not match the position of PDS 70c given in Benisty et al. (2021). In addition, these spurs are roughly aligned with the elongated beam in IB17, and they are absent in LB19, suggesting that they are imaging artefacts.

The non-detection of PDS 70c in IB17 (Fig. 4d) places a 3σ upper limit on its flux density of $89 \mu\text{Jy}$. Since its flux in LB19 is $(126 \pm 16.4) \mu\text{Jy beam}^{-1}$, if we assign the upper limit flux density to PDS 70c in IB17, then it brightened by $42\% \pm 13\%$ in the interval of ~ 1.75 yr between IB17 and LB19. This might not be so surprising since stellar, and probably also sub-stellar, accretion is thought to be variable. Indeed, Szulágyi & Ercolano (2020) report a variability of the $\text{H}\alpha$ flux from CPDs in the range 28% to 58%, over a time-scale of ~ 3 yr. Perhaps the signal stemming from PDS 70c is due to the free-free emission concomitant to the $\text{H}\alpha$ detection. If so, its spectral index should be $\alpha \sim 0.7$ (Wright & Barlow 1975), and should be more conspicuous relative to the disc at lower frequencies.

Alternatively, the signal detected in LB19 might be due to dust being heated up by episodic accretion, if it has time to heat-up in 1.75 yr. Using the dust mass estimates from Benisty et al. (2021) and Portilla-Revelo et al. (2022), the Rosseland opacities from Casassus et al. (2019b), and for a flat surface density out to 1 au in radius, the vertical Rosseland optical depth of this CPD would be in the range 5 to

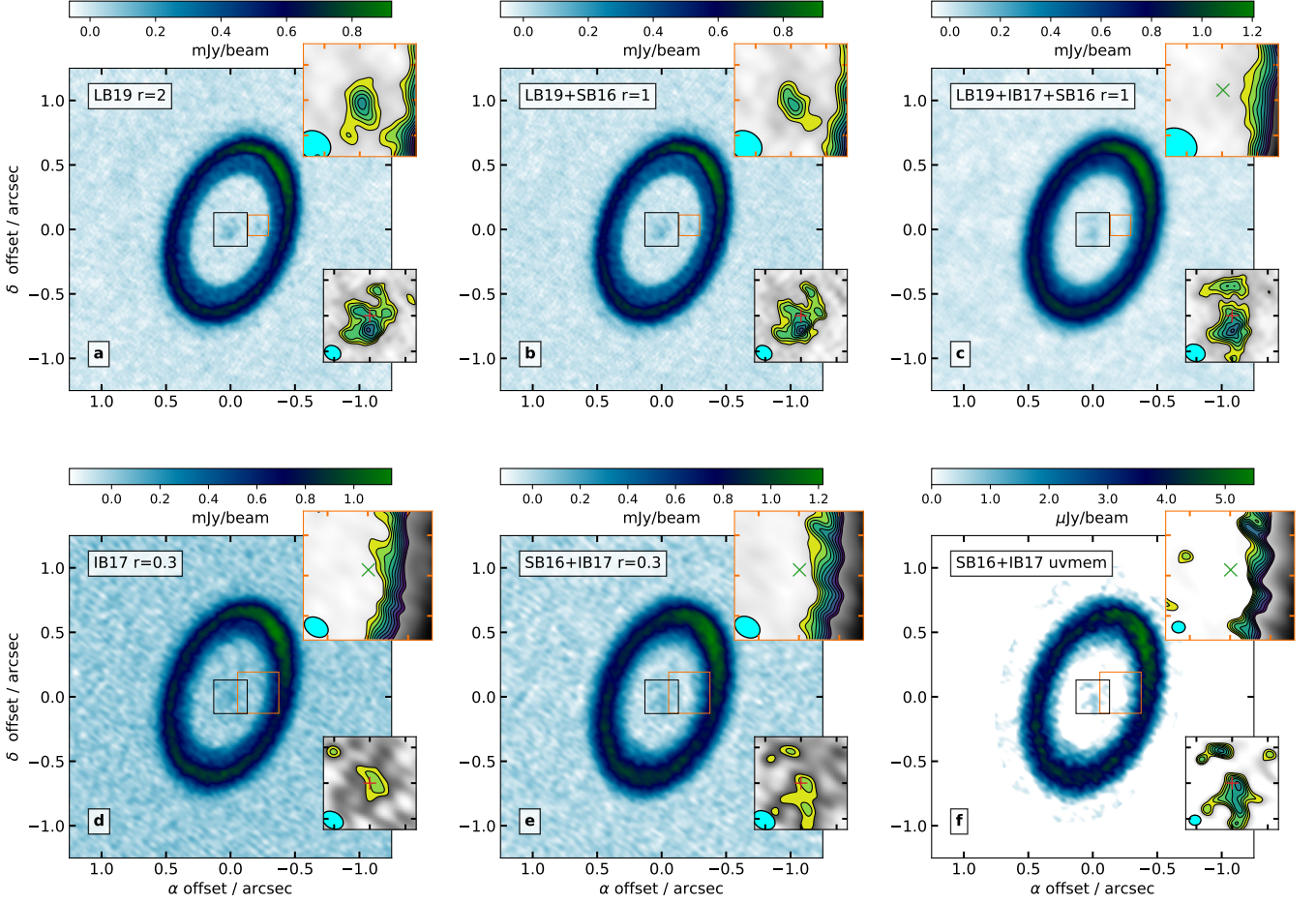


Figure 4. Multi-configuration imaging at 351 GHz in PDS 70. **a:** Restored UVMEM image for LB19, with Briggs robustness parameter $r = 2.0$, resulting in a clean beam of $\Omega_b = 0''.048 \times 0''.039 / 59^\circ$, where we give the beam major axis (bmaj), minor axis (bmin) and direction (bpa) in the format bmaj**×**bmin/bpa. The noise in the residual image is $\sigma = 16.4 \mu\text{Jy beam}^{-1}$. The two insets zoom on the central region, with tick-marks separated by $0''.1$, and on PDS 70c, with tick-marks at $0''.05$. In both insets the linear grey scale stretches over the range of intensities in each region, and the contour levels start at 3σ and are incremented in units of σ . Intensities within each contour level are color-coded differently. **b:** same as a) but for the concatenation LB19+SB16, with $\Omega_b = 0''.048 \times 0''.039 / 58^\circ$, and $\sigma = 15.7 \mu\text{Jy beam}^{-1}$. **c:** same as a) but for the concatenation LB19+SB16+IB17, with $\Omega_b = 0''.058 \times 0''.047 / 58^\circ$, and $\sigma = 15.8 \mu\text{Jy beam}^{-1}$. **d:** Same as a) but for IB17, restored with $r = 1$, with $\Omega_b = 0''.078 \times 0''.064 / 59^\circ$, and $\sigma = 29.6 \mu\text{Jy beam}^{-1}$. In the inset centered on PDS 70c, the tick marks are separated by $0''.1$, and the green cross marks the position of PDS 70 at the epoch of IB17. **e:** Same as c) but for SB16+IB17, restored with $r = 0.3$, with $\Omega_b = 0''.067 \times 0''.049 / 60^\circ$, and $\sigma = 31.9 \mu\text{Jy beam}^{-1}$. **f:** UVMEM model image for SB16+IB17, with an approximate resolution of $1/3$ the natural weight beam (Cárcamo et al. 2018), or $\Omega_b \approx 0''.033 \times 0''.029 / 88^\circ$. The contours start at 3σ , where $\sigma = 0.1 \mu\text{Jy pix}^{-1}$ is a representative noise level.

5000, depending on maximum grain size and temperature. The corresponding radiative diffusion crossing time is at most 1 month, so much shorter than the timescale for the H α variability.

3.2.3 The inner disc

Another interesting feature of the available data in PDS 70 is the structure of the inner disc, which appears to be even more statistically significant than the detection of PDS 70c. The face-on view in Fig. 7b, obtained with the disc orientation given above, shows extended substructure in the inner disc, with a peak at 8σ (labeled ‘Clump 1’ in Fig. 7). Intriguingly, Clump 1 is offset from the ring center by $\sim 0''.03$ to $0''.04$, which is comparable to the natural-weights beam. At

such small angular scales we expect Keplerian rotation to result in detectable morphological changes in the time-span of ~ 1.75 yr between IB17 and LB19. For a $\sim 0.9 M_\odot$ star (Keppler et al. 2019), and at a distance of 113.4 pc, material at a radius of $0''.04$ (4.5 au) would rotate by 62° , or 95° at $0''.03$ (3.4 au). In Fig. 7a we choose the SB16+IB17 UVMEM model image (from Fig. 4f) for a comparison with LB19, as it has a similar angular resolution as SB16+LB19. Since the statistical properties of the model image are not well constrained, the comparison is tentative. We find Clump 1 offset by $\sim 70^\circ$ in azimuth relative to SB16+LB19, as expected for Keplerian rotation if the centre of mass coincides with the ring center. The V-shaped structure with Clump 1 at its vertex appears to rotate as a rigid body, which might reflect a wave launched by Clump 1. However, in IB17 another peak,

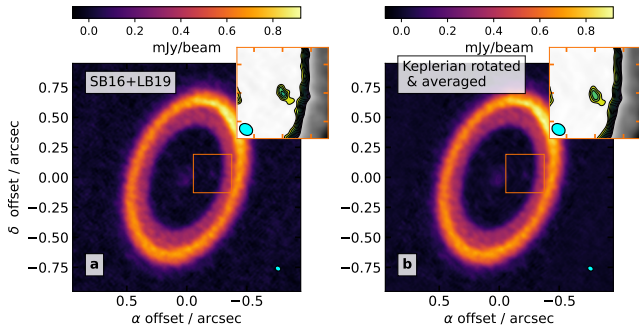


Figure 5. The impact of Keplerian rotation over a time-span of 1.75 yr. **a)** Restored image for LB19+SB16, same as Fig. 4b but for a different color scheme. **b)** Average of the image in a), and its transformation to a Keplerian phase rotated by 1.75 yr.

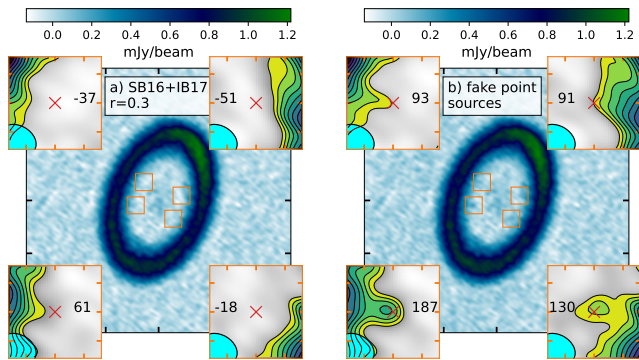


Figure 6. Tests of point source sensitivity through the injection of point sources in IB 17. **a):** same as Fig. 4e, but with 4 insets that zoom in on the expect position of PDS 70c, and 3 other locations, at symmetrical positions relative to the disc axes. The red crosses mark the centre of each inset, and the numbers close to the red crosses correspond to the specific intensity value at the cross. **b):** same as a), but with the addition of fake $126 \mu\text{Jy}$ point sources at all 4 locations.

labeled Clump 2 in Fig. 7, more compact and that reaches the same peak intensity as Clump 1, is found offset by $\sim 0''.08$. Keplerian rotation on a circular orbit would be insufficient to bring Clump 2 to its position in LB19; perhaps it is on a eccentric orbit and/or it is rapidly infalling. If Clump 2 is indeed the same structure in both epochs, it is fainter relative to Clump 1 in LB19.

The signal from the inner disc appears to be featureless in the images from Benisty et al. (2021, their Figs. 2 or 3 for Briggs $r=1$, or their Fig. 6 for Briggs $r=2$). A possible explanation for this difference could be that the structures picked-up here are part of the residuals in Benisty et al. (2021). For instance the bulk of the inner disc may have been fit by a medium-scale Gaussian component in multi-scale *tclean*, while the details of the structure would have required deeper cleaning. These residuals would have been down-scaled by the JvM correction (see Sec. A5), and the inclusion of the extended multi-scale *tclean* component on this central emission may have resulted in a seemingly featureless inner disc.

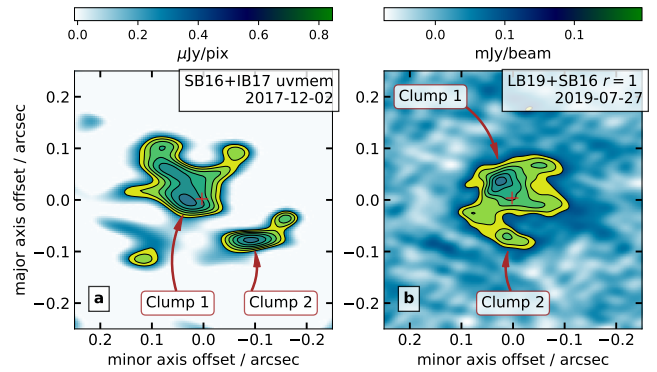


Figure 7. Face-on views of the inner disc in PDS 70. Disc rotation is retrograde (clock-wise). The plus sign marks the origin and coincides with the ring center for each image. The x -axis and y -axis are aligned with the disc minor and major axis, respectively. **a)** Restored image for LB19+SB16 (from Fig. 4b, with the same contours and noise levels). **b)** UVMEM image from Fig. 4f.

4 CONCLUSIONS

In this article we have revisited the ALMA data on PDS 70 using a different imaging strategy than that in the original publications. We used the synthesis imaging package UVMEM, which is an alternative to *tclean*. We have coupled UVMEM to the standard self-calibration procedure implemented in CASA, within a programming framework called OOSELF-CAL. We also proposed a strategy for multi-epoch joint image restoration, which requires the alignment of the visibility data. This alignment was performed in the uv -plane and implemented in the VISALIGN package.

As a result of the application of VISALIGN and OOSELF-CAL to the available data in PDS 70, we have reached the following conclusions:

- (i) The point source in PDS 70c is detected, but only at the 8σ level.
- (ii) The same point source is absent in IB17, suggesting that it is variable by $42\% \pm 13\%$ on 1.75 yr timescales.
- (iii) The inner disc of PDS70 is structured and variable. Its peak is offset by $\sim 0''.04$ from the ring center. We tentatively observe that the peak appears to rotate according to Keplerian rotation relative to the ring center.

We caution on the use of the JvM correction, which was applied in the original publication of the long-baseline observations of PDS 70. The JvM correction exaggerates the peak-signal to noise ratio of the restored images by a factor of up to ten.

ACKNOWLEDGEMENTS

We thank the referee, Prof. Stéphane Guilloteau, for a thorough review and constructive comments that improved the manuscript, as well as for fixing an error in the extraction of the power spectra in Figs. 2 and 3. We also thank Jonathan Williams and Sebastián Pérez for readings of the manuscripts and useful comments. We acknowledge the help of the DASK and ASTROPY communities for their technical support in the

development of VISALIGN and PYRALYSIS. S.C. and M.C. acknowledge support from Agencia Nacional de Investigación y Desarrollo de Chile (ANID) given by FONDECYT Regular grants 1211496, ANID PFCHA/DOCTORADO BECAS CHILE/2018-72190574 and ANID project Data Observatory Foundation DO210001. This paper makes use of the following ALMA data: ADS/JAO.ALMA#2015.1.00888.S, 2017.A.00006.S, 2018.A.00030.S. ALMA is a partnership of ESO (representing its member states), NSF (USA) and NINS (Japan), together with NRC (Canada), MOST and ASIAA (Taiwan), and KASI (Republic of Korea), in cooperation with the Republic of Chile. The Joint ALMA Observatory is operated by ESO, AUI/NRAO and NAOJ.

DATA AVAILABILITY

The reduced ALMA data presented in this article are available upon reasonable request to the corresponding author. The original or else non-standard software packages underlying the analysis are available at the following URLs: MPOLARMAPS (<https://github.com/simoncasassus/MPolarMaps>, Casassus et al. 2021b), UVMEM (<https://github.com/miguelcarcamov/gpvmem>, Cárcamo et al. 2018), PYRALYSIS (<https://gitlab.com/miguelcarcamov/pyralysis>), VISALIGN (<https://github.com/simoncasassus/VisAlign>), OOSELFICAL (https://github.com/miguelcarcamov/objectoriented_selfcal).

REFERENCES

- Andrews S. M., et al., 2021, *ApJ*, **916**, 51
 Benisty M., et al., 2021, *ApJ*, **916**, L2
 Briggs D. S., 1995, PhD thesis, New Mexico Institute of Mining and Technology
 Briggs D. S., Schwab F. R., Sramek R. A., 1999, in Taylor G. B., Carilli C. L., Perley R. A., eds, *Astronomical Society of the Pacific Conference Series Vol. 180, Synthesis Imaging in Radio Astronomy II*, p. 127
 Brittain S. D., Najita J. R., Carr J. S., 2019, *ApJ*, **883**, 37
 Cabrera G. F., Casassus S., Hitschfeld N., 2008, *ApJ*, **672**, 1272
 Cárcamo M., Román P. E., Casassus S., Moral V., Rannou F. R., 2018, *Astronomy and Computing*, **22**, 16
 Casassus S., Cabrera G. F., Förster F., Pearson T. J., Readhead A. C. S., Dickinson C., 2006, *ApJ*, **639**, 951
 Casassus S., et al., 2015, *ApJ*, **811**, 92
 Casassus S., et al., 2018, *MNRAS*, **477**, 5104
 Casassus S., et al., 2019a, *MNRAS*, **483**, 3278
 Casassus S., Pérez S., Osses A., Marino S., 2019b, *MNRAS*, **486**, L58
 Casassus S., Vidal M., Arce-Tord C., Dickinson C., White G. J., Burton M., Indermuehle B., Hensley B., 2021a, *MNRAS*, **502**, 589
 Casassus S., et al., 2021b, *MNRAS*, **507**, 3789
 Chael A. A., Johnson M. D., Bouman K. L., Blackburn L. L., Akiyama K., Narayan R., 2018, *ApJ*, **857**, 23
 Christiaens V., et al., 2019, *MNRAS*, **486**, 5819
 Cornwell T., Fomalont E. B., 1999, in Taylor G. B., Carilli C. L., Perley R. A., eds, *Astronomical Society of the Pacific Conference Series Vol. 180, Synthesis Imaging in Radio Astronomy II*, p. 187
 Czekala I., et al., 2021, *ApJS*, **257**, 2
 Event Horizon Telescope Collaboration et al., 2019a, *ApJ*, **875**, L1

- Event Horizon Telescope Collaboration et al., 2019b, *ApJ*, **875**, L4
 Francis L., Johnstone D., Herczeg G., Hunter T. R., Harsono D., 2020, *AJ*, **160**, 270
 Haffert S. Y., Bohn A. J., de Boer J., Snellen I. A. G., Brinchmann J., Girard J. H., Keller C. U., Bacon R., 2019, *Nature Astronomy*, **3**, 749
 Högbom J. A., 1974, *A&AS*, **15**, 417
 Isella A., Benisty M., Teague R., Bae J., Keppler M., Facchini S., Pérez L., 2019, *ApJ*, **879**, L25
 Jorsater S., van Moorsel G. A., 1995, *AJ*, **110**, 2037
 Keppler M., et al., 2019, *A&A*, **625**, A118
 Long Z. C., et al., 2018, *ApJ*, **858**, 112
 McMullin J. P., Waters B., Schiebel D., Young W., Golap K., 2007, in Shaw R. A., Hill F., Bell D. J., eds, *Astronomical Society of the Pacific Conference Series Vol. 376, Astronomical Data Analysis Software and Systems XVI*, p. 127
 Öberg K. I., et al., 2021, *ApJS*, **257**, 1
 Pearson T. J., et al., 2003, *ApJ*, **591**, 556
 Portilla-Revelo B., Kamp I., Rab C., van Dishoeck E. F., Keppler M., Min M., Muro-Arena G. A., 2022, *A&A*, **658**, A89
 Rau U., Cornwell T. J., 2011, *A&A*, **532**, A71
 Remijan A., et al., 2019, *ALMA Technical Handbook*, ALMA Doc. 7.3, ver. 1.1, 2019, [doi:10.5281/zenodo.4511522](https://doi.org/10.5281/zenodo.4511522)
 Shepherd M. C., 1997, in Hunt G., Payne H., eds, *Astronomical Society of the Pacific Conference Series Vol. 125, Astronomical Data Analysis Software and Systems VI*, p. 77
 Sutton E. C., Wandelt B. D., 2006, *ApJS*, **162**, 401
 Szulágyi J., Ercolano B., 2020, *ApJ*, **902**, 126
 Szulágyi J., Plas G. v. d., Meyer M. R., Pohl A., Quanz S. P., Mayer L., Daemgen S., Tamburello V., 2018, *MNRAS*, **473**, 3573
 Thompson A. R., Moran J. M., Swenson George W. J., 2017, *Interferometry and Synthesis in Radio Astronomy*, 3rd Edition, [doi:10.1007/978-3-319-44431-4](https://doi.org/10.1007/978-3-319-44431-4)
 Wiaux Y., Jacques L., Puy G., Scaife A. M. M., Vanderghelynst P., 2009, *MNRAS*, **395**, 1733
 Wright A. E., Barlow M. J., 1975, *MNRAS*, **170**, 41

APPENDIX A: IMAGE RESTORATION

A1 Motivation for image restoration, and for a reconsideration of the JvM correction

The interpretation of radio interferometer observations usually involves a model of the sky image that accounts for the visibility data (except in the direct measurement of power spectra, e.g. Pearson et al. 2003). These models are often parametric (e.g. Event Horizon Telescope Collaboration et al. 2019a). Such parametric models describe the source with few parameters, and if the model is an adequate representation of the source, their posterior distributions can be used to assess uncertainties. However, in general the model image is non-parametric. The traditional synthesis imaging algorithm CLEAN uses a collection of compact sources, represented by spikes or circular Gaussians, and distributed by matching-pursuit (Högbom 1974; Rau & Cornwell 2011). A variety of Bayesian image synthesis algorithms, or more generally regularized maximum likelihood optimizations of the model image, have been proposed. Some use a regular grid to represent the model image, which is then referred to as the ‘deconvolved image’, as in the UVMEM package (Casassus et al. 2006; Cárcamo et al. 2018), or in ‘Closure Imaging’ (Chael et al. 2018; Event Horizon Telescope Collaboration et al. 2019b), while others use the Voronoi tessellation (Cabrera et al. 2008) or compressed sensing (e.g. Wiaux et al. 2009).

However, the model images by themselves usually lack noise estimates. This is because the inverse problem in image synthesis, i.e. the production of a model image from sparse Fourier data, is intrinsically ill-posed. After gridding the visibility data (see Sec. A3 below), the number of free parameters reach around a million to cover continuously the uv -plane, and exceeds the number of independent data points. Estimates of the uncertainties in the model image are therefore challenging (but see Sutton & Wandelt 2006; Casassus et al. 2015).

As an alternative, to convey the uncertainties in synthesis imaging it is customary to “restore” the model images (e.g. Thompson et al. 2017; Briggs et al. 1999) by convolution with an elliptical Gaussian, which represents the interferometer angular resolution, and the addition of the “dirty map” of the residuals, which is essentially the inverse Fourier transform of the gridded visibility residuals. These residuals encapsulate both the thermal noise and synthesis-imaging artefacts. They may also include faint signal that was missed in the model.

However, there are several different definitions of the dirty map, that correspond to different gridding and data weighting strategies. This degree of freedom has led to a reconsideration of the dirty map units used in standard packages, in the so-called ‘JvM correction’ (Jorsater & van Moorsel 1995; Czekala et al. 2021), resulting in noise values that differ from the standard definition in image restoration. The dirty map of the residuals is then scaled by the ratio of the dirty and clean beams, thereby artificially down-scaling the noise level by up to one order of magnitude. This appendix serves as a caution on the JvM correction, which is increasingly applied in the recent literature (e.g. Benisty et al. 2021; Andrews et al. 2021; Öberg et al. 2021, and the series of articles derived from the MAPS ALMA Large Programme).

A2 Definition of the restored image

We assume that a model image $I_m(\vec{x})$, defined onto a regular grid, has been obtained so that the associated model visibilities $\{V_m(\vec{u}_j)\}_{j=1}^P$,

$$V_m(\vec{u}_j) = \int I_m(\vec{x}) e^{2\pi i \vec{u}_j \cdot \vec{x}} dxdy, \quad (\text{A1})$$

match the observed visibility data $\{V(\vec{u}_j)\}_{j=1}^P$ according to some criterion (for instance a least-squares fit). To simplify notation we have omitted from Eq. A1 the modulation by the primary beam and by the Jacobian of the direction cosines (which are both close to unity in the application to PDS 70c). The residual visibilities are $V_R(\vec{u}_j) = V(\vec{u}_j) - V_m(\vec{u}_j)$. Given a model image and a telescope angular resolution represented by an elliptical Gaussian $g_b(\vec{x})$, the restored image for a single pointing is

$$I_R = I_m * g_b + R_D, \quad (\text{A2})$$

where $R_D(\vec{x})$ is the dirty map of the gridded residual visibilities, $\{\tilde{V}_R(\vec{u}_k)\}_{k=1}^N$, i.e. after averaging the sparsely sampled uv -data into a regular grid with N cells and weights $\{W_k\}_{k=1}^N$. For an extension of Eq. A2 to mosaics see, for example, Casassus et al. (2021a).

A3 Gridding

Since the visibility data correspond to the Fourier transform of the sky image, a first approximation of the sky signal can be obtained by averaging the visibility data into a regular grid and performing the inverse Fourier transform. When this gridding procedure does not extrapolate to the uv -cells devoid of data, which are assigned zero weight, the result is called a dirty map.

There are several techniques for visibility gridding (e.g. Thompson et al. 2017; Briggs et al. 1999). Its simplest version is a straight-forward application of counts in cells to grid the visibility data $\{V_j\}_{j=1}^P$ in a regular grid in the uv -plane, with $N = n \times m$ cells (for a model image defined on an $n \times m$ grid):

$$\tilde{V}_k = \frac{\sum_{i=1}^{N_k} w_i V_i}{\sum_{i=1}^{N_k} w_i}, \quad (\text{A3})$$

where N_k is the number of visibilities that fall in cell (u_k, v_k) and $P = \sum_{k=1}^N N_k$. The weights w_i are propagated to the gridded visibilities, \tilde{V}_k , whose weights are then

$$W_k = \sum_{i \in k} w_i. \quad (\text{A4})$$

There is a wide range of different choices for the visibility weights $\{w_j\}_{j=1}^P$, with different units and resulting in different intensity scales in the corresponding dirty maps (see Sec. A4). Natural weights (e.g. Thompson et al. 2017; Briggs et al. 1999) assign the usual thermal noise weight to each visibility datum:

$$w_i = \omega_{\text{nat},i} = \frac{1}{\sigma_i^2}. \quad (\text{A5})$$

Other weighting schemes are often used to control the effective interferometer resolution. In uniform weights (e.g. Thompson et al. 2017; Briggs et al. 1999) all cells are assigned the same weight, which is achieved by redefining the weight for each datum:

$$w_i = \frac{\omega_{\text{nat},i}}{W_k}, \quad (\text{A6})$$

where W_k is the natural weight of the k -th cell where visibility (u_i, v_i) falls. For uniform weights, Eq. A4 gives the weight of each uv -cell:

$$W_k = \sum_{i \in k} w_i \equiv 1. \quad (\text{A7})$$

In Briggs weighting (Briggs 1995),

$$\begin{aligned} w_i &= \frac{\omega_{\text{nat},i}}{1 + W_k f^2} \\ f^2 &= \frac{(5 \cdot 10^{-r})^2}{\frac{\sum_k W_k^2}{\sum_i \omega_{\text{nat},i}}}, \end{aligned} \quad (\text{A8})$$

where r is the Briggs robustness parameter ($r = 2$ is almost equivalent to natural weights, $r = -2$ is close to uniform weights).

The gridded weights W_k derive from Eq. A4 using the weights w_i , adjusted from the original weights $\omega_{\text{nat},i}$ according to Eqs. A5, A6 or A8. Thus the units for W_k are different for each scheme.

A4 Dirty map, Dirty beam

The dirty map might be thought of as a uniquely defined image, which would be the Fourier pair of the gridded visibilities. However, the degree of freedom in the choice of weighting scheme leads to different units for the dirty map. We therefore adopt the following definition for the dirty map:

$$I_D(x, y) = \sum_k \alpha W_k \tilde{V}_k e^{-2\pi i(u x + v y)} \Delta u \Delta v, \quad (\text{A9})$$

where α is a constant that sets the units for I_D . In order to determine α we consider a point source with flux density F at the phase center. We extract its flux from the gridded visibilities using a least-squares fit,

$$\chi^2 = \sum_k (\tilde{V}_k - \tilde{V}_k^m)^* (\tilde{V}_k - \tilde{V}_k^m) W_k, \quad (\text{A10})$$

where $\tilde{V}_k^m = F$. The root of $\frac{\partial \chi^2}{\partial F} = 0$ is

$$F = \frac{1}{2} \frac{\sum_k (V_o + V_o^*) W_k}{\sum_k W_k}. \quad (\text{A11})$$

Assuming that each visibility datum is independent, the error on F is

$$\sigma_F = \frac{1}{\sqrt{\sum_k W_k}}. \quad (\text{A12})$$

On the other hand, the uncertainty on $I_D(\vec{x} = \vec{0})$ from Eq. A9 is

$$\sigma_I = \alpha \Delta u \Delta v \sqrt{\sum_k W_k^2 \sigma_k^2} = \alpha \Delta u \Delta v \sqrt{\sum_k W_k}. \quad (\text{A13})$$

Next we assume that the uv -coverage is sufficient to use the dirty map to approximate the sky image, smoothed by an elliptical Gaussian that represents the image resolution. This requires that the distribution of weights in the uv -plane is approximately Gaussian, so that its Fourier pair is also an elliptical Gaussian in the image plane, the so-called “clean” beam g_b with full-width-at-half-maximum major and minor axes BMAJ and BMIN, and that subtends a solid angle $\Omega_b = \frac{\pi}{4 \log(2)} \text{BMAJ} \times \text{BMIN}$. Given the degree of freedom in the weighting scheme, there is no uniquely defined clean beam for a given visibility dataset, and neither is there a unique angular resolution. In fact, even for the same weighting scheme, different synthesis imaging packages do not yield the same angular resolution.

If the units for I_D are set to $\text{Jy } \Omega_b^{-1}$, then for a point source at the phase center, with flux density F , we should have

$$\frac{\sigma_I}{[\text{Jy } \Omega_b^{-1}]} = \sigma_F \quad (\text{A14})$$

We can then solve for α :

$$\alpha = \frac{1}{\sum_k W_k \Delta u \Delta v}. \quad (\text{A15})$$

The dirty map, in units of $\text{Jy } \Omega_b^{-1}$, is therefore:

$$I_D(x, y) = \sum_k \frac{W_k}{\sum_l W_l} \tilde{V}_k e^{2\pi i(u x + v y)}, \quad (\text{A16})$$

as is standard. As an example, we consider the dirty map of a unit spike at the phase center, which corresponds to the dirty-map response, or point-spread function (PSF), and is usually called the “dirty beam”:

$$B(x, y) = \sum_k \frac{W_k}{\sum_l W_l} e^{2\pi i(u x + v y)}. \quad (\text{A17})$$

As another example, we consider the case of a perfect instrument with uniform uv -coverage, that fills the uv -grid, with arbitrarily deep data and constant weights W_k . In this case the dirty beam should be a unit spike, and rather than an elliptical clean beam we would use the solid angle subtended by a pixel in the sky image, $\Omega_b = \Delta x \Delta y$, so that Eq. A16 yields the same spike in units of Jy pix^{-1} .

We have checked that the synthesis imaging packages CASA (McMullin et al. 2007) and DIFMAP (Shepherd 1997) produce dirty maps with consistent units. This can be confirmed by simulating visibility data onto a unit spike in the absence of noise, and deriving the corresponding dirty map (using task `tclean` in CASA or `mapplot` in DIFMAP), which yields peak intensities of unity. In fact the dirty map of a unit spike is of course just the dirty-map PSF and is one of the default products of tasks `tclean` and `mapplot`.

A5 The JvM correction

For consistency with the flux scale set by the visibility data (Eq. A11), the dirty map, as defined by Eq. A16, bears units of $\text{Jy } \Omega_b^{-1}$, where Ω_b is the “clean” beam. By contrast, in the JvM correction (Jorsater & van Moorsel 1995; Czekala et al. 2021), a ‘dirty beam’ solid angle, here denoted by Ω_D , is introduced to represent the solid angle subtended by the dirty map of a point source, and to set the units of the dirty map in Eq. A16 to $\text{Jy } \Omega_D^{-1}$. In this context, for image restoration the residual dirty map must be scaled by the beam ratio $\epsilon = \text{Jy } \Omega_b^{-1} / \text{Jy } \Omega_D^{-1}$ before addition with the convolved model image.

However the solid angle integral for Ω_D will in general not converge, as acknowledged by Czekala et al. (2021), and which can readily be concluded from Fig. 1 in (Jorsater & van Moorsel 1995). These authors propose instead two different solutions to estimate ϵ . In the original formulation of the JvM correction, Jorsater & van Moorsel (1995) solve for ϵ by comparing the total flux density extracted in a region between two versions of the restored images. These two versions can be different depths of cleaning, or simply the dirty and clean maps. However, the convolution with dirty beam sidelobes will bias the flux density, in ways that depend on the flux extraction aperture. In turn, Czekala et al. (2021) adopt a different definition for Ω_D and ϵ . They propose to perform an azimuthal average of the dirty beam, and truncate the radial domain of the dirty beam solid angle integral to the first null in the radial direction.

In both versions of the JvM correction the values for ϵ range from 1 to 1/10, and the extreme corresponds to natural weights. But both choices seem arbitrary, either in the definition of the flux extraction aperture, or in the choice of domain for the solid integral. Neither options are consistent with the requirement set by Eq. A14, since they both re-scale the units for the dirty maps. The result is an artificial increase of sensitivity by up to a factor of $1/\epsilon$.

The original motivation of the JvM correction may perhaps stem from the normalisation of the dirty beam: since the dirty beam is the dirty map response to a unit spike, it may be thought that its peak intensity should correspond to the point source flux for the ‘correct beam solid angle’. But this argument breaks down if the integrated flux diverges.

This paper has been typeset from a $\text{\TeX}/\text{\LaTeX}$ file prepared by the author.